

Optical Engineering

OpticalEngineering.SPIEDigitalLibrary.org

Error compensation for long-distance measurements with a photoelectric autocollimator

Renpu Li
Igor Konyakhin
Quan Zhang
Wei Cui
Dandan Wen
Xinhai Zou
Junqi Guo
Yu Liu

Error compensation for long-distance measurements with a photoelectric autocollimator

Renpu Li,^a Igor Konyakhin,^b Quan Zhang,^a Wei Cui,^a Dandan Wen,^a Xinhai Zou,^a Junqi Guo,^a and Yu Liu^{a,*}

^aChongqing University of Post and Telecommunications, Chongqing Engineering Research Center of Intelligent Sensing Technology and Microsystem, Chongqing, China

^bITMO University, Faculty of Applied Optics, St. Petersburg, Russia

Abstract. Although autocollimators enable noncontact measurement, their performance is limited in large-scale and long-distance applications because of errors caused by nonideal point light sources. Therefore, we analyze this type of measurement error, including the error source and the equations used to describe the irradiance distribution of the light spot. A two-dimensional exponential approximation formula is used to express the light irradiance distribution and compensate the spot imaging errors. Experimental results show that the measurement error could be reduced by sixfold. Therefore, the proposed compensation algorithm can be applied to autocollimator measurements over distances. © The Authors. Published by SPIE under a Creative Commons Attribution 4.0 Unported License. Distribution or reproduction of this work in whole or in part requires full attribution of the original publication, including its DOI. [DOI: 10.1117/1.OE.58.10.104112]

Keywords: photoelectric autocollimator; long-distance measurement; error compensation.

Paper 190915 received Jul. 10, 2019; accepted for publication Oct. 16, 2019; published online Oct. 31, 2019.

1 Introduction

The autocollimator is an important angle measuring instrument¹⁻⁶ that enables noncontact measurement with high accuracy and high resolution. However, the performance of this instrument is limited in large-scale and long-distance applications because of the autocollimator's physical characteristics and operating principle, and this limitation prevents use in many prominent areas, such as ship and aircraft manufacturing and generator and radar monitoring.⁷ Because the measurement range of the photoelectric autocollimator is closely related to the measurement distance,⁸ long-distance and wide-range autocollimator has become a significant research focus in recent years.⁹⁻¹³

Chen et al.¹² proposed an angle measurement method based on optical frequency domain and realized a measurement range of 21,600 arc sec. Li et al.⁹ employed a cube corner as a reflector to extend the angle measurement range from 1.2 deg to 12 deg with an accuracy better than 35 arc sec. Zhu et al.¹³ proposed a common-path design criterion for laser-datum based on measurement of small angle deviations, and this approach realized high-precision measurement at long distances. However, these methods have large measurement errors when used for far ranging. The main cause of these errors is that the optical beam is not uniform due to the nonideal point source.¹⁴

Therefore, this paper analyzes the measurement error caused by an uneven light beam under long working distance conditions. An algorithm is proposed to compensate the error and thereby increase the measurement accuracy. The algorithm is verified by experiments that demonstrate a sixfold reduction in the error under long-distance conditions.

2 Model Principle and Analytical Methods

A schematic of a typical photoelectric autocollimator is shown in Fig. 1. A light emission diode is used as the source

of radiation source, and the autocollimator projects a collimated beam onto a planar reflector that is mounted on a target at distance L . The autocollimator unit measures the tilt angle of the target by detecting the deviation of the reflected beam with respect to the projected beam's axis. The beam is deflected by a beam splitter (BS), collimated by a collimating lens (CL), and then projected onto the reflector. The reflected beam from the reflector is focused by CL, passed through the BS and propagates to the photoelectric sensor, which is a complementary metal-oxide-semiconductor (CMOS) matrix used to measure the displacement between the source and reflection of the focused laser light spot.

The photoelectric autocollimator is a precision instrument for small-angle measurement, and the tilting of the target will change the displacement of the reflected light spot on the CMOS. Although this measurement principle is based on a point light source, the light source is not actually a point light source, and this discrepancy causes measurement errors over long distances, as follows.

A schematic of the radiation component of the autocollimator is shown in Fig. 2.

The radius of the light source is a . A Lambertian approximation can be used for the condition $f \gg a$, where f is the focal length of the CL. The beams from every point of the light source are collected by the CL at an angle β with the main optical axis CL. The largest value of β is a divergence angle β_m , which can be expressed as

$$\beta_m = \arctg(a/f). \quad (1)$$

The whole optical path can be divided into two regions, the internal region I and the external region II. This area is determined by beams B , b and C , c , which radiate from the bottom and top of the point source, respectively.

Each point in region I has the same irradiance, and thus region I can be defined as the uniform irradiance region, within which lies the optimal position of the reflector. The length of the nearest part of region I from the point

*Address all correspondence to Yu Liu, E-mail: liuyu@cqupt.edu.cn

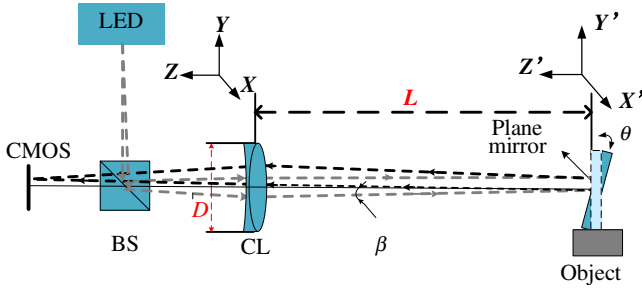


Fig. 1 Schematic of a typical photoelectric autocollimator.

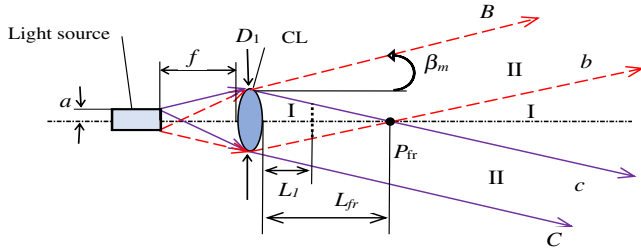


Fig. 2 Schematic of the radiation component of an autocollimator.

P to the CL is L_{fr} ,¹⁴ which is defined as the formation distance of the beams. L_{fr} can be calculated by

$$L_{fr} = \frac{D_1}{2 \cdot \tan(\beta_m)} = \frac{D_1 \cdot f}{2 \cdot a}, \quad (2)$$

where D_1 is the diameter of the CL.

In a conventional autocollimator, the reflector is located at the formation distance L_1 not more than formation distance L_{fr} , the illumination of the entire image is uniform, and beams radiated from all point sources will be imaged on the CMOS. As shown in Fig. 1, the reflector is indicated by the dotted line.

The working distance L_1 can be expressed as

$$L_1 = \frac{D_2 - D_3}{2 \cdot \tan(\beta_m)} = \frac{(D_2 - D_3) \cdot f}{2 \cdot a}, \quad (3)$$

where D_3 is the diameter of reflector 3. In general, a conventional photoelectric autocollimator has $D_1 = 50$ mm, $D_3 = 30$ mm, $f = 500$ mm, and $a = 0.25$ mm. The reflector 3 is the entrance pupil of the optical system path. Applying these specifications to Eq. (3), the working distance of a typical photoelectric autocollimator is 10 m, which significantly limits its application.

To expand the working distance of the photoelectric autocollimator, we place the entrance pupil of the optical system in region I behind the point P_{fr} , namely, $L_2 > L_{fr}$. The equivalent optical path diagram in which the CL2' is the image of the lens 2 by the reflector 3 as shown in Fig. 3.

When the diameter of the reflector is $D_3 \geq D_1$, CL2' is the entrance pupil of the optical system path. As shown in Fig. 3, the working distance L_2 of the autocollimator can be expressed as

$$L_2 = 2L_{fr}. \quad (4)$$

Equation (4) shows that the maximum range of the autocollimator can reach 100 m.

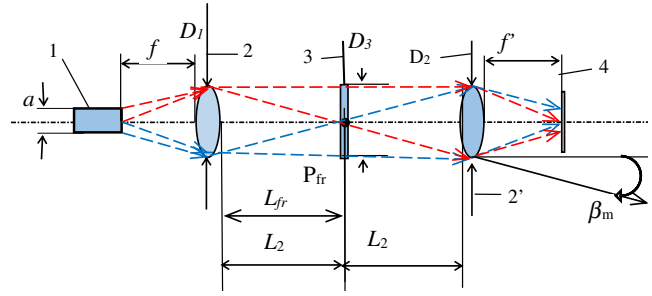


Fig. 3 Schematic diagram of working distance L_2 : 1, light source; 2, CL; 3, reflector; 2', image of the CL; and 4, CMOS.

When $L_2 > L_{fr}$, the light beam from the radiant point is limited by the diameter of reflector 3 or the CL, which completely block the main part of the radiation beams B, b and C, c at the boundary of the light source. Because of this vignetting, the irradiance on the imaging plane is no longer uniform and becomes less symmetrical when the mirror rotates, which causes measurement errors.¹⁴

2.1 Measurement Error Caused by Beam Limitation

The irradiance distribution on the imaging surface must be analyzed when the reflector is located behind the beam formation distance to determine to what extent the angle measurement error is caused by the beam limitation. To study the imaging of a beam on the CMOS under this condition, the diameter of D_3 is assumed to be larger than that of the CL, D_1 (and D_2), as in Fig. 4: $D_3 > D_1$ and $D_3 > D_2$. A diagram of the optical path with then entrance pupil of the optical system located behind L_{fr} , is shown in Fig. 4.

As can be seen from Fig. 4, the beams from the light source are collimated by CL2 and projected onto the reflector R, and then the reflected beams are focused by CL2' onto the CMOS4, with most of the energy focused on the point O. As seen in Fig. 5, a radiant point at a distance r from the center O of the light source generates the radiation beam that is inclined at an angle of β to the main optical axis. At this

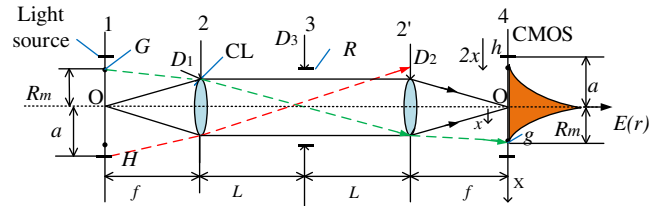


Fig. 4 Diagram of the optical path with beam limitation.

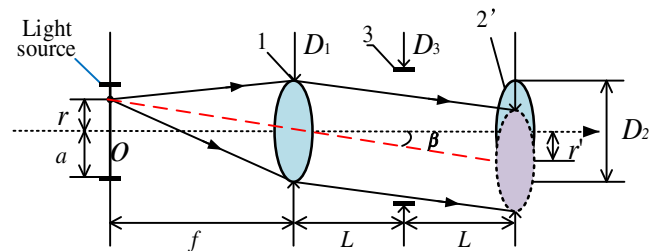


Fig. 5 Partial off-axis beam displacement at the aperture plane of the objective lens.

point, some off-axis beams passing through CL2, with a diameter of D_1 , will be irradiated on the equivalent CL2'. The displacement of the facula relative to the equivalent objective lens is r' , which can be expressed as

$$r' = 2 \cdot L \cdot \operatorname{tg}(\beta), \quad (5)$$

where β is the divergence angle between the off-axis beam and the main optical axis.

The irradiance value on the imaging plane of the off-axis beams is proportional to the area of intersection between the aperture of CL2' and the off-axis beam. This intersection area is smaller than the aperture size of the on-axis beam. Therefore, the irradiance of the facula formed by the off-axis beam on the imaging plane is less than that at the point of O .

The optical path in Fig. 4 shows that the irradiance $E(r)$ on the CMOS plane is distributed from the maximum point $E(0)$ to the minimum point g , attenuating according to a certain law. The distance from g to the central coordinate of the CMOS plane is $r = R_m$.

The final imaging on the CMOS is shown in Fig. 6. The area circumscribed by radius a is not the sum of the imaging of all the radiant points on the source; rather, it is the sum of the imaging of the radiant points R_m from the center point of the source. The irradiance of point g on the imaging plane corresponding to the point g in Fig. 4 is O .

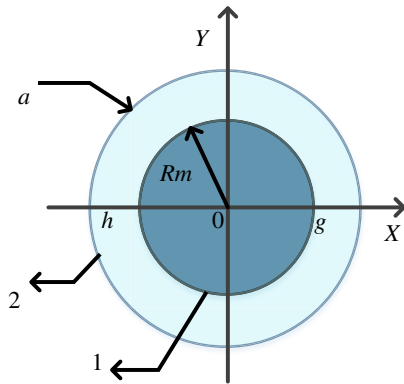


Fig. 6 Image plane when reflector is at rest: the number 1 represents the image boundary of the light source on the CMOS, and the number 2 represents the corresponding circumference of the light source boundary.

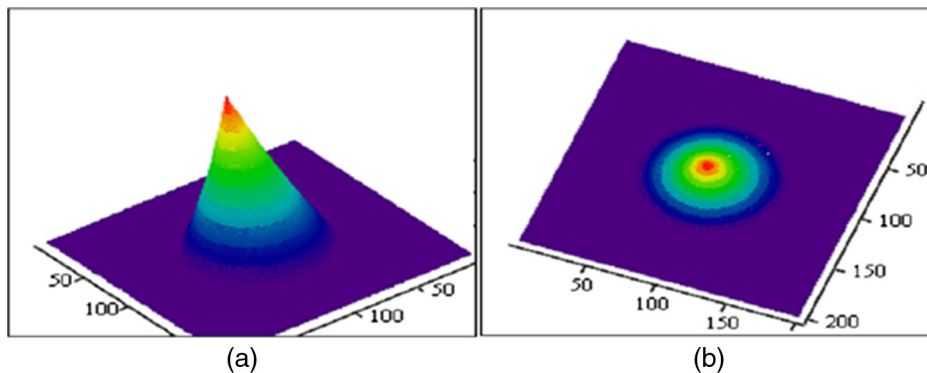


Fig. 7 Three-dimensional form of image irradiance in different fields of view when the reflector plane is at rest - (a) Tilt 40 deg, Twist 125 deg, (b) Tilt 80 deg, Twist 160 deg.

According to the light path of the radiant point g from the light source, the corresponding point of g on the imaging plane can be found, and the following relation can be obtained:

$$R_m = \frac{D \cdot f}{2 \cdot L}. \quad (6)$$

The irradiance of the corresponding image surface can be calculated as¹⁵

$$E(r) = \frac{2}{\pi} \left\{ \arccos[\gamma(r)] - \sqrt{1 - [\gamma(r)]^2} \cdot \gamma(r) \right\}, \quad (7)$$

$$\gamma(r) = \frac{r}{R_m}, \quad 0 < r < R_m. \quad (8)$$

By calculating the $E(r)$ function, a two-dimensional imaging pattern of $E(r)$ can be obtained as shown in Fig. 7.

2.2 Calculation of the Measurement Error Caused by the Different Tilt Angles of the Reflector Plane

When the reflector plane deflects a tilt angle of θ in relation to the main optical axis, the displacement of the imaging circle can be expressed as

$$x = f \cdot \operatorname{tg}(\theta). \quad (9)$$

However, the reflected beam will be deflected from the main optical axis at an angle of 2θ after the collimating beams have been reflected by a deflected reflector. In this case, the displacement of the aperture of the radiant point at the image edge on the image plane can be expressed as

$$\tilde{x} = f \cdot \operatorname{tg}(2 \cdot \theta) \approx 2 \cdot x. \quad (10)$$

In Fig. 8, when the displacement of the light source boundary (circle 2) with respect to the image boundary (circle 1) is greater than l_0 , a part of the image is eliminated, and the irradiance distribution of the image is no longer symmetrical. The value of l_0 can be expressed by the following equation:

$$l_0 = \tilde{x} - x = a - R_m. \quad (11)$$

For a tilt angle θ_0 , the corresponding irradiance displacement can be found by identifying the root of the following equation:

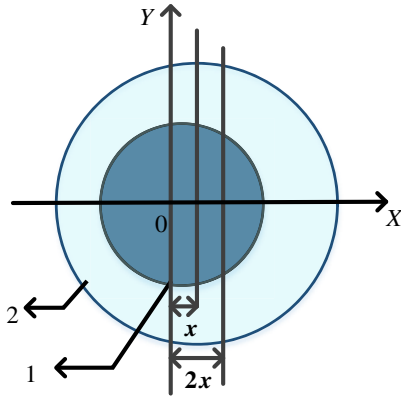


Fig. 8 Image contour of the light source with a tilted reflector plane: the number 1 represents the image boundary of the light source on the CMOS, and the number 2 represents the corresponding circumference of the light source boundary.

$$\frac{tg(\theta_0)}{\cos(2 \cdot \theta_0)} = \frac{a}{f} - \frac{D_c}{2 \cdot L}. \quad (12)$$

The unevenness of the constricted image and corresponding irradiance energy distribution causes a discrepancy between the displacement x_c of the energy center of the image and the image displacement x in Eq. (9). Because the photoelectric sensor of the autocollimator directly measures the displacement x_c of the energy center of the image, the measurement error caused by

$$\sigma_{\Theta} = \arctg\left(\frac{x}{f}\right) - \arctg\left(\frac{x_c}{f}\right) \approx (x - x_c)/f. \quad (13)$$

In order to simplify the calculation of the error value, the image boundary can be considered to have a fixed location and only the light source boundary is displaced by a distance x from the center. Figure 9 shows the relative position of the light source boundary and the image boundary.

In this case, the value of the energy center of the constricted image is equal to the measurement error of the image displacement, which can be expressed as

$$\hat{x}_c = x_c - x. \quad (14)$$

In fact, the coordinates of the energy center of the constricted image are equal to the difference in Eq. (13).

Referencing the coordinate axis in Fig. 9, the coordinates of the energy center in Eq. (14) can be expressed as

$$\hat{x}_c = \frac{\int_0^{F_2(x,y)} [\int_{-b_1}^{-b_2} x \cdot E(x,y) dx] dy}{\int_0^{F_2(x,y)} [\int_{-b_1}^{-b_2} E(x,y) dx] dy} + \frac{\int_0^{F_1(x,y)} [\int_{-b_2}^0 x \cdot E(x,y) dx] dy}{\int_0^{F_1(x,y)} [\int_{-b_2}^0 E(x,y) dx] dy} + \frac{\int_0^{F_1(x,y)} [\int_0^{R_m} x \cdot E(x,y) dx] dy}{\int_0^{F_1(x,y)} [\int_0^{R_m} E(x,y) dx] dy}. \quad (15)$$

In Eq. (15), b_1 and b_2 are the points on the OX coordinate axis, $F_1(x,y)$ expresses the image boundary, $F_2(x,y)$

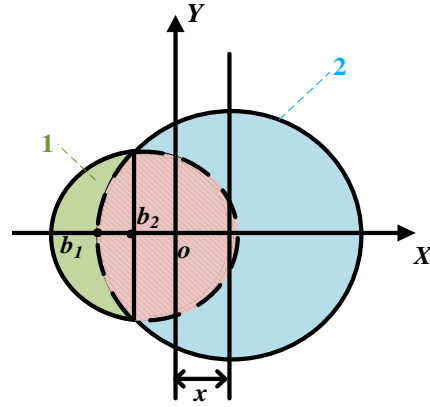


Fig. 9 Relative position of the light source boundary 2 and the image boundary 1.

expresses the light source boundary conjugate circle, and $E(x,y)$ expresses the two-dimensional irradiance distribution of the image, yielding the result of Eq. (7) in the case of $r = \sqrt{x^2 + y^2}$. However, because of the complexity of the integrand in Eq. (15), $E(x,y)$ is not suitable for the study of the measurement error relationship.

Therefore, an approximation of the CMOS analyzer based on Eq. (7) is suggested by the two-dimensional formula $E_e(x,y)$ with a separable variable based on the exponential function:

$$E_e = \exp\left[-\frac{(x+y)}{k \cdot R_m}\right], \quad (16)$$

where R_m is the radius of the image in Eq. (6), and $k = 0.61$ can be found by the two-dimensional exponential approximation $E(x,y)$ and the least squares method. The image surface irradiance distribution obtained by Eq. (16) is shown in Fig. 10.

2.3 Measurement Error Analysis after Using Exponential Function

The image plane model should appropriately change when calculating the irradiance distribution using the exponential approximation formula $E_e(x,y)$. Figure 11 shows a simulation of the image irradiance contour boundary obtained by the exponential approximation function. Here, the image boundary and the corresponding light source boundary are approximately squares.

Figure 12 shows a simulation of the approximation $E_e(x,y)$ of the light irradiance distribution and the contour variation of the image plane in the constricted image. The parameter l , which represents the displacement offset between the image and the edge of the light source, can be expressed as

$$l = x - (R_m - a). \quad (17)$$

Thus the measurement error of the image's energy center will occur only in the case of $l > 0$.

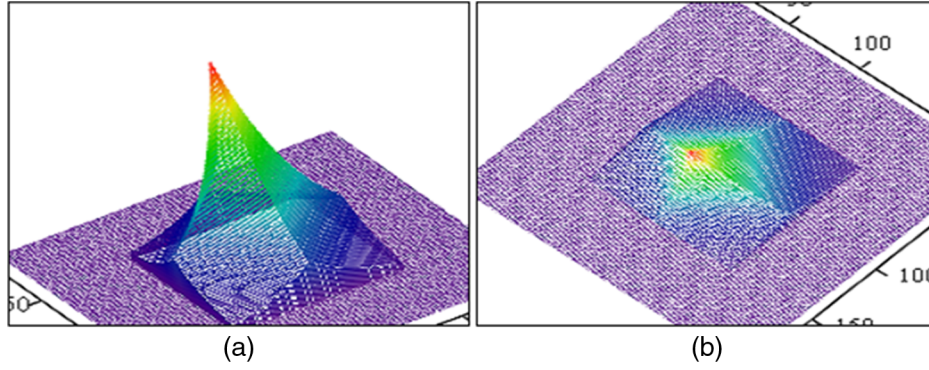


Fig. 10 Irradiance distribution obtained by Eq. (16) in different fields of view - (a) Tilt 30 deg, Twist 135 deg, (b) Tilt 85 deg, Twist 140 deg.

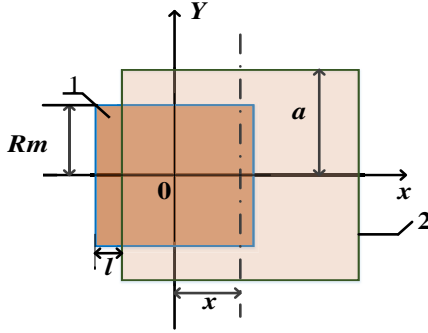


Fig. 11 Image irradiance contour boundary simulated by the exponential approximation function: the number 1 represents the image boundary of the light source on the CMOS, and the number 2 represents the corresponding circumference of the light source boundary.

The error of the image coordinates at $l < R_m$ is given by

$$\hat{x}1_c = \frac{\int_0^{R_m} [\int_{-(R_m-l)}^0 x \cdot E_e(x, y) dx] dy}{\int_0^{R_m} [\int_{-(R_m-l)}^0 E_e(x, y) dx] dy} + \frac{\int_0^{R_m} [\int_0^{R_m} x \cdot E_e(x, y) dx] dy}{\int_0^{R_m} [\int_0^{R_m} E_e(x, y) dx] dy}. \quad (18)$$

When $l > R_m$, the error is given by

$$\hat{x}2_c = \frac{\int_0^{R_m} [\int_{(l-R_m)}^0 x \cdot E_e(x, y) dx] dy}{\int_0^{R_m} [\int_{(l-R_m)}^0 E_e(x, y) dx] dy}. \quad (19)$$

We can obtain the expected expression of the measurement error of the image coordinates after substituting Eq. (16) into Eqs. (17)–(19). The measurement error is normalized using the parameter R_m , which is the radius of the image on the photo sensor to compute the formula:

$$\sigma_x = \frac{\tilde{x}_c}{R_m}. \quad (20)$$

When $l < R_m$, this value can be obtained from Eq. (18):

$$\sigma_1 = \frac{e^{\frac{q}{k}} \cdot (q - k - 1) + (k + 1)}{e^{\frac{q}{k}} - 2 \cdot e^{\frac{2}{k}} + 1}. \quad (21)$$

When $l > R_m$, the value can be obtained from Eq. (19):

$$\sigma_2 = \frac{e^{-\frac{q}{k}} \cdot e^{\frac{2}{k}}(k + q - 1) - (k + 1)}{e^{-\frac{q}{k}} \cdot e^{\frac{2}{k}} - 1}. \quad (22)$$

Here $k = 0.61$ is the parameter of the approximation $E_e(x, y)$ in Eq. (16), and q is the measured displacement l of the image after normalization by R_m , which can be expressed as

$$q = \frac{l}{R_m}. \quad (23)$$

The normalized function graph of σ_1 and σ_2 is shown in Fig. 13. The computer simulations indicated that the difference between the irradiance distributions obtained by the suggested approximation and by the exact formula did not

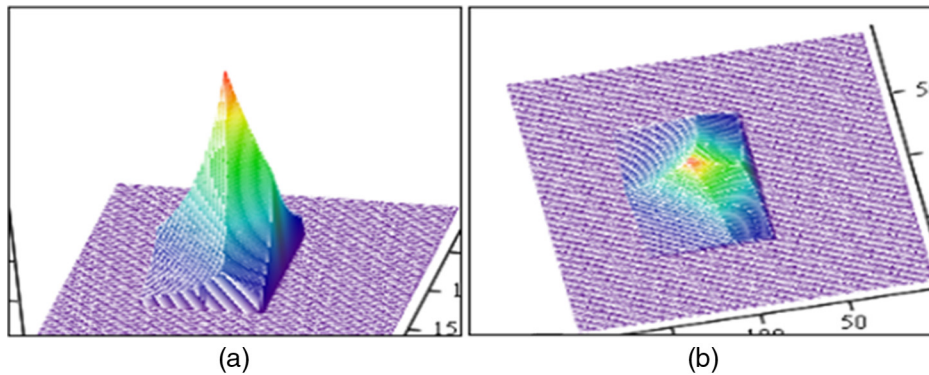


Fig. 12 Irradiance distribution of the image in different fields of view - (a) Tilt 40 deg, Twist 165 deg, (b) Tilt 85 deg, Twist 185 deg.

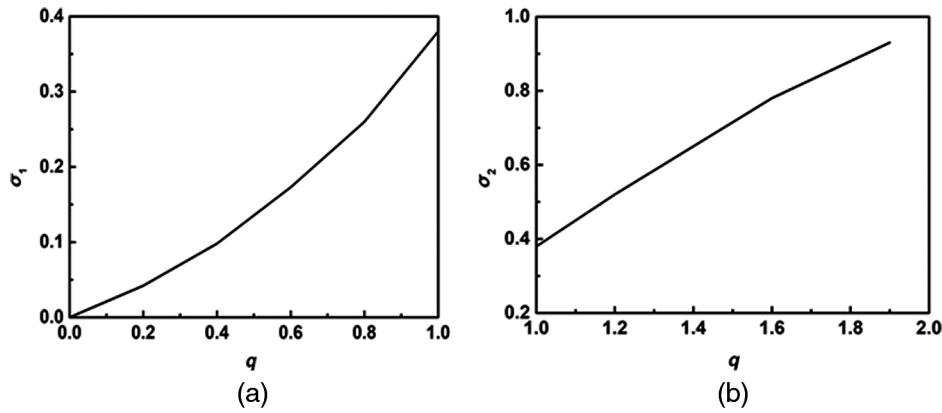


Fig. 13 Normalized errors in the displacement measurement when: (a) $q < l$ and (b) $q > l$.

exceed 5% few percent, demonstrating the reliability of the proposed model.

3 Results of Experimental Comparison

The aberrations of the objective lens CL 2 and the uneven refractive index of the optical components, air turbulence, and temperature variations all lead to measurement errors of the photoelectric autocollimator. However, since a high-quality objective lens is used in the photoelectric autocollimator, the aberration is extremely small compared to the size of the image on the CMOS and can be ignored. The measurement error caused by the uneven refractive index of the optical component is smaller because the measurement beam is always completely filled with the entrance pupil of the objective lens when measured by the photoelectric autocollimator. In the process of measurement, if the stability of the ambient temperature can be maintained and the nonturbulent airway is ensured, the influence of the external environmental test will be reduced. Therefore, the main cause of the measurement error of the photoelectric autocollimator of this experiment is the measurement error caused by the vignetting phenomenon of the beam caused by the aperture of the optical component.

3.1 Experimental Study on Compensation for Errors Caused by Beam Limitation

The experimental platform consisted of a tested photoelectric autocollimator, high-precision calibrated standard photoelectric autocollimator TriAngle TA 1000-140 produced from Germany Trioptics GMBH, corresponding two reflectors, Laser Tracker API Radian 80 and corresponding cube-corner reflector.

As shown in Fig. 14, the tested photoelectric autocollimator 1 and laser tracker 3 are placed in rigid flat platform 4. The reflectors 6 and 7 of autocollimators 1 and 2 are perpendicular to each other and they are rigidly connected with rotary table 5. The rotary table 5, cube-corner reflector 8 of the laser tracker, and high-precision standard autocollimator 2 are fixed with rigid base 9. The rigid platform 4 and the rigid base 9 are installed on the concrete walls of two adjacent rooms, respectively. The distance between the rigid platform 4 and rigid base 9 is 20.5 m, and the distance from the objective lens of the photoelectric autocollimator 2 to the reflector 7 is 0.2 m. The cube-corner reflector 8 is always kept static to monitor rigid base 9 no linear displacement.

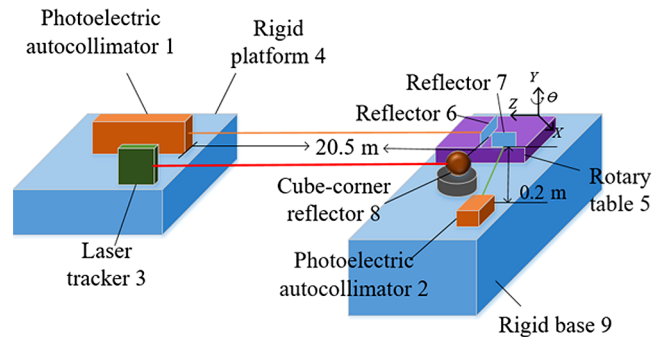


Fig. 14 The structure of experiment table.

The linear position stability of the rigid base 9 is measured by a laser tracker with an error of 0.05 mm. The rotation angle of the rotary table 5 is measured by the autocollimator 2, and the measurement error is 0.2 arc sec. The stability of the experimental environment including air humidity, temperature, and air pressure is monitored by laser tracker 3. The air temperature is $21^{\circ}\text{C} \pm 0.2^{\circ}\text{C}$ in the experimental time.

This experiment was tested several times from 1 to 4 a.m. In order to eliminate the influence of environmental factors on the measurement results, we repeat the measurement process when using a laser tracker to monitor environmental changes. Finally, we compared the environmental changes during several measurements and selected a set of measurements in the most stable environment. The CMOS of the photoelectric autocollimators 1 and 2 measures the imaging spot of each measuring angle 10 times and then takes the average value of the data as the final measured value of the angle. This approach avoids the effects of air interference on measurement errors. In the first stage of the experiment, we gave the artificial tilting angle of the reflector 6 and 7 along the Y axis through the rotary table 5. The tilting angle is measured by autocollimators 1 and 2 at the same time.

In the second stage of the experiment, we established an image processing algorithm based on the proposed model and repeated the first stage of the experiment to obtain the error results. The correctness of the compensation method was verified by the comparative analysis of the two results.

The distance between the photoelectric autocollimator 1 and the reflector 6 is larger than the beam formation distance L_{fr} in Fig. 2. The measurement distance of the experimental photoelectric autocollimator needs to reach 20.5 m, and the

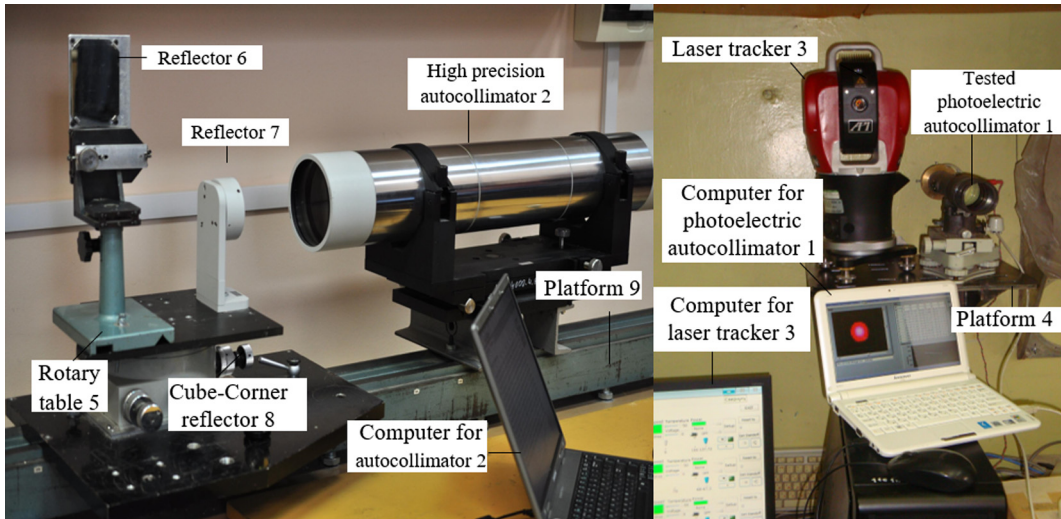


Fig. 15 Experimental sample picture of high-precision autocollimator and the rotating platform with the plane reflector and photoelectric autocollimator with laser tracker.

measurement range needs to reach 4.5 arc min with an accuracy error requirement of not more than 2 arc sec. The objective lens of the autocollimator that we used had a 400-mm focal length, a 55-mm caliber, and a circle of confusion of 0.02-mm in diameter. The autocollimator has a circle of confusion of 0.02-mm in diameter and a 0.6-mm light source

radius. The light source was a semiconductor diode SFH 485 P with a power of 10 mw, the photoelectric sensor was a OV05620 CMOS QSXGA with a 2592×1944 resolution and a pixel size of $2.2 \times 2.2 \mu\text{m}^2$, and the reflector 6 had a size $75 \times 100 \text{ mm}^2$ (Fig. 15).

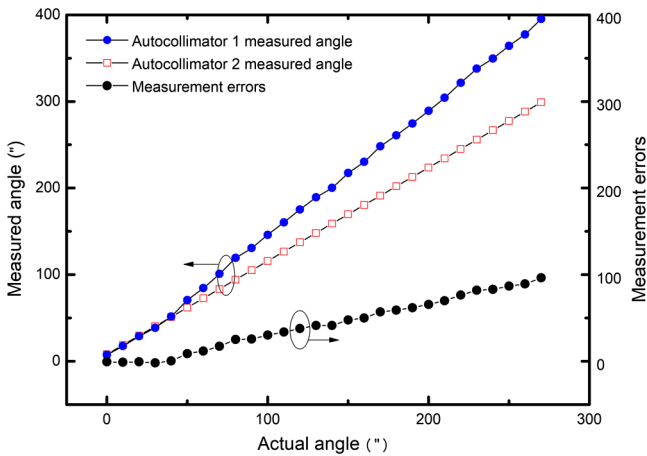


Fig. 16 Measured angles and measurement errors.

3.2 Experimental Results

In the experiments, we gave the rotary table 5 at tilting angle θ , ranging from 0 to 4 arc min 30 arc sec, in intervals of 10 arc sec. Figure 16 shows the performance of the transducer function of autocollimator $\theta_t = \Phi(\theta)$. On the horizontal axis, θ is the tilting angle of the reflector. On the vertical axis, θ_t is the angle measured by the autocollimator.

The error of a measurement $\sigma\theta$ was the difference between the tilting angle θ of high-precision photoelectric autocollimator 2 and the tested photoelectric autocollimator 1 measured angle θ_t :

$$\sigma\theta = \theta_t - \theta. \tag{24}$$

In Fig. 16, θ is shown by the red cube, and the error $\sigma\theta$ is shown by the black circles.

Figure 17 shows the imaging spot of the light source on the CMOS when the reflector was static and when the

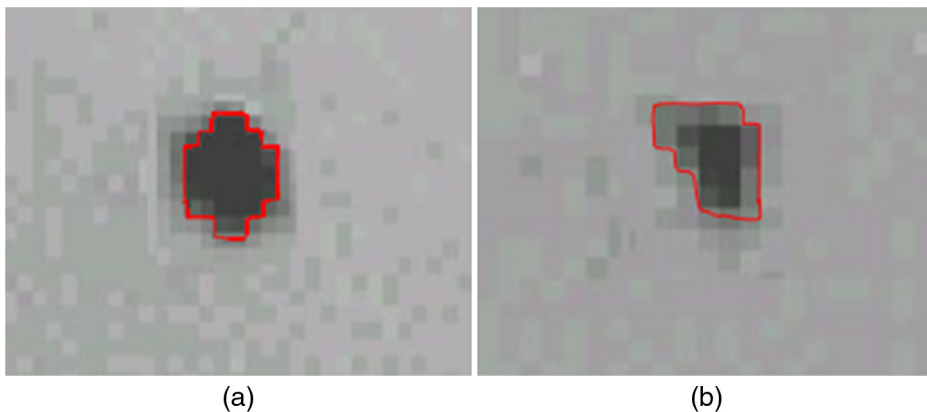


Fig. 17 Image on CMOS: (a) static reflector and (b) reflector rotated by 200 arc sec.

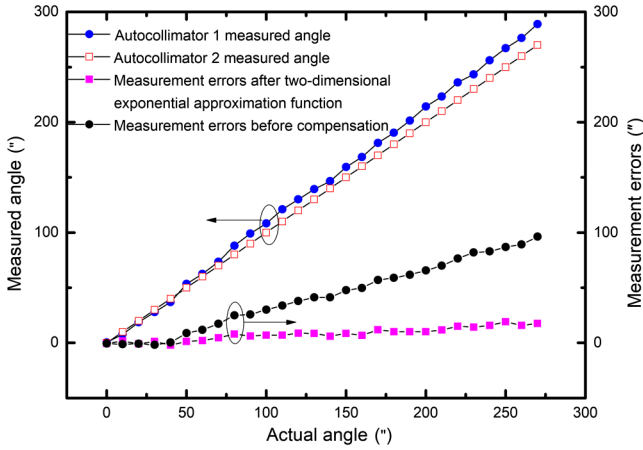


Fig. 18 Measurement performance.

reflector was rotated by 200 arc sec. The above images verify the error generation mechanism proposed in this paper.

The measurement error is made up of both systematic and random errors. The systematic error of the image can be approximated as $\sigma\theta = \Phi(\theta)$. The systematic error of the photoelectric autocollimator is almost zero when the tilt angle of the reflector is not more than $\theta_0 = 30$ arc sec, as is the case when Eq. (11) does not exceed its limit. The initial experiment showed that the systematic error reaches 35% of the output value without the compensation algorithm.

Figure 18 shows the results of the second stage of the experiment, when the compensation formula was applied to the calculation results of Eqs. (21) and (22), representing the θ_t measured by the autocollimator. The performance of the transducer function $\theta_{\text{corr}} = \Phi(\theta)$ of autocollimator is shown by the curved line.

In Fig. 18, the blue circles represent the measured angle θ_t of autocollimator 1 and the red cubes represent the measured angle θ_t of autocollimator 2. Compensated measurement error $\sigma\theta$ is shown by the pink cube, and the black circles show the error before the compensation.

According to Eq. (12), when the measured value θ exceeds the value θ_0 , the error compensation algorithm was used, and the R_m parameter of the image on the CMOS was calculated according to Eq. (6). The compensation algorithm included the following steps.

1. The rotary table rotates θ and the measurement angle of the high-precision autocollimation is θ . Then the measurement value of the autocollimator contains the measurement error $\sigma\theta$:

$$\hat{\theta} = \theta + \sigma\theta. \quad (25)$$

In the expression, the measured values θ and $\sigma\theta$ are independent of each other.

2. We can calculate the displacement value \hat{x} of the image by $x = f \cdot \text{tg}(\theta)$ according to the measurement angle θ . This value contains the measurement error value \hat{x}_c of the image coordinates:

$$\hat{x} = x + \hat{x}_c. \quad (26)$$

In the expression, the measured values x and \hat{x}_c are independent of each other.

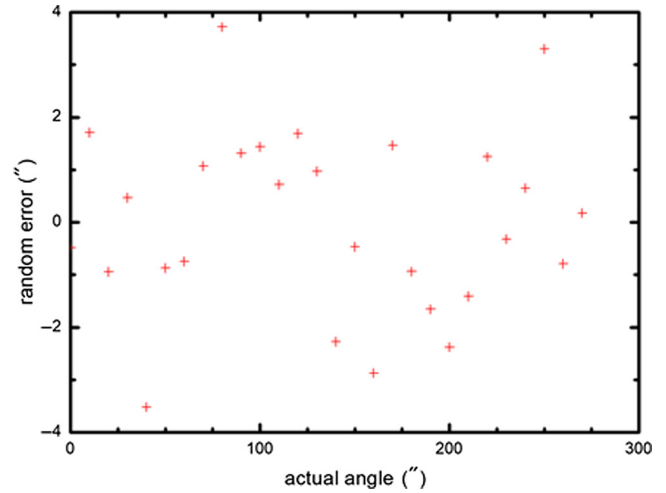


Fig. 19 Measurement of random error.

3. We can calculate the value \hat{l} by $l = x - (R_m - a)$ according to the value θ . This value contains the measurement error value \hat{x}_c :

$$\hat{l} = l + \hat{x}_c. \quad (27)$$

In the expression, the measured values l and \hat{x}_c are independent of each other.

4. Equation (26) is divided by the obtained R_m , and an expression is obtained according to Eq. (23). The calculation of \hat{q} is as follows:

$$\hat{q} = q + \sigma_x(q). \quad (28)$$

The parameters \hat{q} are obtained from the measurement angle $\hat{\theta}$ of the autocollimator, where the mathematical meaning of $\sigma_x(q)$ is expressed by Eqs. (21) and (22). Equation (27) is thus a nonlinear equation.

5. The value q can be calculated by Eq. (27), and the value of l can be calculated by Eq. (23).
6. Find the l value and the \hat{x}_c value by Eq. (26), and use them to calculate the value x of the image according to Eq. (25).
7. Then through Eq. (9), the accurate measurement θ_t after the error compensation can be obtained.

From the experiment results, the systematic error after compensation is $<6\%$. The error of measurement $\sigma\theta$ was linearly fitted as $\delta\theta$, and the difference $\sigma\theta - \delta\theta$ was considered the random error as shown in Fig. 19. The standard deviation of measurement error of is ~ 2 arc sec.

Although the random error remains the same as before the compensation, this experiment demonstrated that the proposed compensation algorithm can effectively compensate the measurement error caused by the beam limitation of the photoelectric autocollimator.

4 Conclusion

In this paper, we analyzed the measurement errors produced by the nonideal point light sources of photoelectric autocollimators used over long distances. Through the error

analysis, the influence of vignetting on the measurement was elucidated, and then the error was compensated using a known two-dimensional approximation formula. However, the complexity of the formula made the compensation impossible, and we, therefore, proposed a two-dimensional exponential approximate formula to analyze and compensate the spot imaging. Through experimental verification, this algorithm was shown to effectively reduce the error caused by the nonideal point source in the long-distance measurements of the photoelectric autocollimator.

Acknowledgments

This work was supported the National Key R&D Program of China (Nos. 2018YFF01010202 and 2018YFF01010201); the National Natural Science Foundation of China (Nos. 61705027, 11704053, 61901069, and 51902037); Government of the Russian Federation (Grant No. 08-08); the Innovation Leader Talent Project of Chongqing Science and Technology (No. CSTC-CXLJRC201711), the Basic Research Project of Chongqing Science and Technology Commission (Nos. CSTC-2017csmsA40017 and CSTC-2018jcyjx0619); and the Science and Technology Project Affiliated to the Education Department of Chongqing Municipality (Nos. KJZH17115 and KJQN201800626).

References

1. V. Heikkinen et al., "Interferometric 2-D small angle generator for autocollimator calibration," *Metrologia* **54**(3), 253–261 (2017).
2. T. Yandayan et al., "Investigations of interpolation errors of angle encoders for high precision angle metrology," *Meas. Sci. Technol.* **29**(6), 064007 (2018).
3. K. Li, C. Kuang, and X. Liu, "Small angular displacement measurement based on an autocollimator and a common-path compensation principle," *Rev. Sci. Instrum.* **84**(1), 015108 (2013).
4. Y. X. Ni et al., "Optimization design of the angle detecting system used in the fast steering mirror," *Optoelectron. Lett.* **14**(1), 48–52 (2018).
5. O. Novyanto, "An approach method to calibrate the autocollimator with small angle measurement range," *MAPAN-J. Metrol. Soc. India* **31**(1), 9–15 (2015).
6. H. B. Xu et al., "Performance analysis of air-water quantum key distribution with an irregular sea surface," *Optoelectron. Lett.* **14**(3), 216–219 (2018).
7. A. E. Gorodetskiy et al., *Analysis of Errors at Optic-Electronic Autocollimation Control System with Active Compensation*, Studies in Systems, Decision and Control, vol. **49**, pp. 251–258, Springer, Switzerland (2016).
8. A. Konyakhin and T. V. Turgalieva, "Three-coordinate digital autocollimator," *J. Opt. Technol.* **80**(12), 772–777 (2013).
9. R. Li et al., "Cube-corner autocollimator with expanded measurement range," *Opt. Express* **27**(5), 6389–6403 (2019).
10. K. Ishikawa et al., "Profile measurement of aspheric surfaces using scanning deflectometry and rotating autocollimator with wide measuring range," *Meas. Sci. Technol.* **25**(6), 064008 (2014).
11. Y. L. Chen et al., "Mode-locked laser autocollimator with an expanded measurement range," *Opt. Express* **24**(14), 15554–15569 (2016).
12. Y. L. Chen et al., "Optical frequency domain angle measurement in a femtosecond laser autocollimator," *Opt. Express* **25**(14), 16725–16738 (2017).
13. F. Zhu, J. Tan, and J. Cui, "Common-path design criteria for laser datum based measurement of small angle deviations and laser autocollimation method in compliance with the criteria with high accuracy and stability," *Opt. Express* **21**(9), 11391–11403 (2013).
14. R. M. Khusnutdinov, "Effect of light-beam limitation on the measurement error of a tracking photoelectric autocollimator," *Sov. J. Opt. Technol.* **56**(7), 414–416 (1989).
15. D. V. Zhukov, I. A. Konyakhin, and A. A. Usik, "Iterative algorithm for determining the coordinates of the images of point radiators," *J. Opt. Technol.* **76**(1), 36–38 (2009).

Renpu Li received his BS and MS degrees from the ITMO University in 2012 and 2014, respectively, and his PhD in 2017 from the ITMO University. He is currently an assistant professor at the School of Optoelectronic Information of Chongqing University of Post and Telecommunications of China. His research interests include integrated optics and optical system.

Igor Konyakhin received his PhD in autocollimator optoelectronic devices and systems from the Russian State Research University ITMO in 1981. He has been a professor in the Department of Optoelectronic Devices and Systems at the Russian State Research University since 2000. He has published 3 scientific monographs, 37 scientific conference reports, and 93 papers. He is a major member of the Russian Kozhdestvensky Optical Society and member of SPIE.

Quan Zhang majored in communication engineering during his undergraduate study. He is now a sophomore majoring in integrated circuits at Chongqing University of Posts and Telecommunications.

Wei Cui received his master's degree and doctor's degree from the School of Telecommunications at Xi'an Jiaotong University. He took part in joint training at Hokkaido University, Japan, from 2015 to 2016. In 2016, he became a lecturer at Chongqing University of Posts and Telecommunications of Optoelectronics. He mainly engaged in femto-second laser micro-nano-processing technology and fiber-optic sensor components research.

Dandan Wen received her MS and PhD degrees from the University of Electronic Science and Technology in 2012 and 2016, respectively, and her joint doctorate from the School of Electrical and Mechanical Engineering at the University of California, Berkeley. In 2018, she became a lecturer at Chongqing University of Posts and Telecommunications of Optoelectronics.

Xinhai Zou received his doctor's degree of optical engineering from the University of Electronic Science and Technology. Since 2018, he has been engaged in scientific research and teaching at Chongqing University of Posts and Telecommunications.

Junqi Guo graduated from NanKai University in June 2016 and has been working at the School of Optoelectronic Engineering of Chongqing University of Posts and Telecommunications since September 2016. He was a director of Chongqing Intelligent Sensor Innovation Alliance.

Yu Liu is a professor and doctoral supervisor of electronic science and technology at Chongqing University of Posts and Telecommunications. He was named the 300 science and technology innovation talents in Chongqing and other honors. He studies sensor components and systems, including new inertial sensors, multisensor combinations, and information fusion technologies.